Optics Letters

Full-space wavefront control enabled by a bilayer metasurface sandwiching 1D photonic crystal

Yanhao Chu,[1] Chen Chen,[1,2] Xingjian Xiao,[1] Wenjing Shen,[1] Xin Ye,[1] Shining Zhu,[1] and Tao Li[1,3]

[1]National Laboratory of Solid State Microstructures, Key Laboratory of Intelligent Optical Sensing and Manipulation, Jiangsu Key Laboratory of Artificial Functional Materials, College of Engineering and Applied Sciences, Nanjing University, Nanjing 210093, China
[2]chenchen2021@nju.edu.cn
[3]taoli@nju.edu.cn

Received 28 July 2023; revised 14 October 2023; accepted 15 October 2023; posted 16 October 2023; published 6 November 2023

Metasurfaces, composed of sub-wavelength structures, have a powerful capability to manipulate light propagations. However, metasurfaces usually work either in pure reflection mode or pure transmission mode. Achieving full-space manipulation of light at will in the optical region is still challenging. Here we propose a design method of full-space meta-device containing a bilayer metasurface sandwiching 1D photonic crystal to manipulate the transmitted and reflected wave independently. To provide a proof-of-concept demonstration, a device is proposed to show the light focusing in transmission and a vortex beam in reflection. Meanwhile, a device focusing the reflected light with oblique 45° incidence and the transmitted light with normal incidence is designed to indicate its application potential in augmented reality (AR) application. Our design provides a promising way to enrich the multifunctional meta-devices for potential applications.

https://doi.org/10.1364/OL.501949

The modulation of electromagnetic (EM) wavefront has always been a hotspot for researchers. In the past decades, metasurface [1], as a 2D version of the metamaterial, has attracted more and more researchers' interest due to its compact architecture and powerful light modulation capabilities [2]. Many fascinating effects, such as focusing [3–7], holography [8,9], etc., have been realized by metasurfaces, showing great promises in optics applications [10–17].

Nevertheless, metasurfaces usually work either in pure reflection mode [18,19] or pure transmission mode [20,21], leaving half the EM space unutilized. Recently, full-space multifunctional metasurfaces characterized by independent EM manipulation in both transmission and reflection space have been proposed in the microwave region. Specifically, most transmission and reflection integrated metasurfaces (TRIM) utilize two orthogonal polarizations to realize the respective transmission and reflection functions, which makes them polarization dependent [22–29]. Besides, resonant phase and one or more carefully designed polarization selection layers are used in the microwave region TRIM design scheme. Nevertheless, in the optical regions, the resonant phase has severe absorption loss, and the counterpart of the polarization selection layer above is also challenging. Collective interference effects of supercells were also utilized to independently modulate the transmission mode and reflection mode with different circular polarized light incidences [11]. However, the proposed bifacial metasurface is still polarization-sensitive, leaving the function in quite limited scenarios. On the other hand, bilayer metasurfaces with extended design freedom have been showing powerful capabilities in correcting imaging aberrations [30–32] and increasing polarization channels [33]. Such a configuration would possibly provide promising solutions to overcome the TRIM challenge.

In this Letter, we propose a design method for the independent modulation of the transmitted and reflected light in the optical regions. By integrating a bilayer metasurface embedded with a 1D photonic crystal, the designed device can control the transmission wavefront at $\lambda_1 = 1550$ nm and also reshape the reflection wavefront at $\lambda_2 = 1250$ nm, as shown in Fig. 1. More importantly, wavefront modulation in both transmission and reflection modes is polarization independent. The effects of focusing and generating vortices of transmitted and reflected beams are demonstrated by specific phase distribution designs. Simulations with both normal and oblique incidences are also performed to illustrate the excellent phase modulation capability and angle robustness.

Figure 2(a) schematically shows a unit cell of the spaced bilayer metasurface with a 1D photonic crystal inserted in the middle. There are two types of meta-atoms with the same material and height employed in each layer as illustrated in Fig. 2(b). The meta-atoms in the bottom layer and the inserted 1D photonic crystal are embedded in a SU8 layer, and the top layer of metasurface is surrounded by air. The top and bottom layers of the meta-atoms with fourfold symmetry provide the polarization-insensitive propagation phase to meet the requirements of the transmitted and reflected wavefront modulation. The inserted 1D photonic crystal acts as a dichroic filter. The 1D photonic crystals are constructed by stacking high refractive index material amorphous silicon (a-Si) and low refractive index material silicon dioxide (SiO_2) alternatively as shown in Fig. 2(c). By varying the thickness of the two materials in one basic unit of the multilayer structure, the center frequency and the width of the photonic crystal bandgap can be adjusted. Thus, the device can achieve

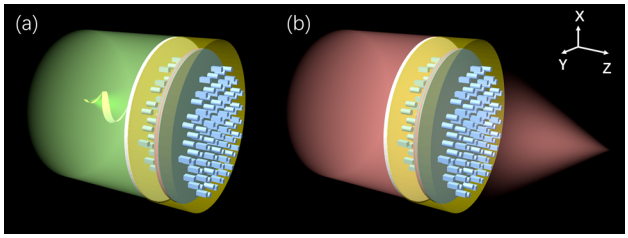

Fig. 1. (a) Schematic of generating vortex beam of reflected wave. (b) Schematic of focusing effect of transmitted wave.

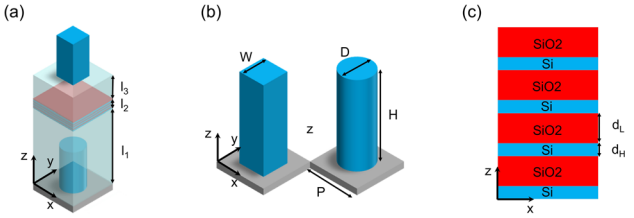

Fig. 2. (a) Schematic of the bilayer nanostructure sandwiching 1D photonic crystal. The thickness of the first layer of SU8 (l_1), the total thickness of the inserted 1D photonic crystal (l_2), and the thickness of the second layer of SU8 (l_3) are shown. (b) Schematics of single-layer meta-atoms of two basic symmetric shapes (circle and square). The height (H), side length (W), diameter (D), and period (P) are shown. (c) Schematic of the 1D photonic crystal alternately stacked by a-Si with thickness (d_H) and SiO_2 with thickness (d_L).

low-frequency transmission and high-frequency reflection or vice versa.

Suppose that a light beam of wavelength λ_1 transmits and a beam of wavelength λ_2 reflects. When a beam of wavelength λ_1 is incident on the device, it will successively pass through the bottom layer of the metasurface, the 1D photonic crystal, and the top layer of metasurface. The phase modulation imposed on the beam at wavelength λ_1 is expressed as $\varphi_{top}(r, \lambda_1) + \varphi_{bottom}(r, \lambda_1)$, where φ_{top} and φ_{bottom} are the phase profile of the top and bottom metasurfaces, respectively. While for a beam of wavelength λ_2, it will be reflected back after passing through the bottom metasurface and be modulated by that once more. The phase modulation imposed on the beam at wavelength λ_2 can be expressed as $2\varphi_{bottom}(r, \lambda_2)$. We denote the phase profile provided by the device in the transmission mode as $\varphi_T(r, \lambda_1)$, and the phase profile in the reflection mode is $\varphi_R(r, \lambda_2)$. To achieve independent modulation of transmission and reflection modes, these terms should satisfy relations as follows:

$$\begin{cases} \varphi_T(r, \lambda_1) = \varphi_{top}(r, \lambda_1) + \varphi_{bottom}(r, \lambda_1) \\ \varphi_R(r, \lambda_2) = 2\varphi_{bottom}(r, \lambda_2) \end{cases}. \quad (1)$$

Specifically, the material of meta-atoms (nanoposts) is set as amorphous silicon (a-Si), which ensures a high modulation efficiency due to its high refractive index and relative high transmission at near-infrared wavelengths even when embedded in a photoresist (SU8) layer. The height of nanoposts (H) is set as 1000 nm, and the unit size (P) is set as 500 nm. The geometry parameters of these structures (such as side length (W) or diameter (D)) are designed in the range of 100 to 400 nm. By employing a commercial software (Lumerical FDTD Solutions), we obtained the electrical field responses in this meta-unit library. The thickness of the first layer of SU8 (l_1) is set to

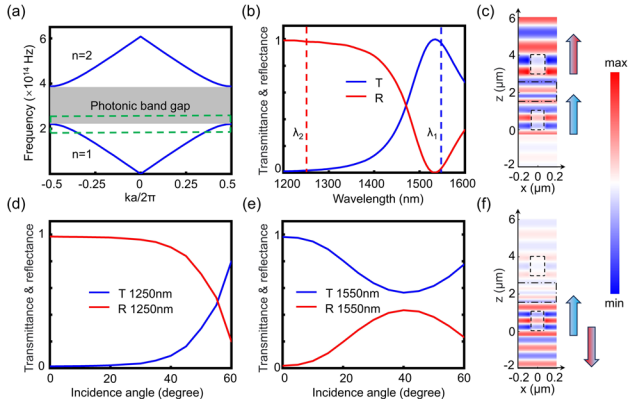

Fig. 3. (a) Energy band diagram of the 1D photonic crystal. The bandgap is identified by a gray rectangle. The green-dotted box highlights the frequency range corresponding to the abscissa value shown in (b). (b) Simulated transmittance and reflectance of the 1D photonic crystal. The red- and blue-dotted lines identify the reflection and transmission operating wavelengths, respectively. Simulated transmittance and reflectance at wavelength 1250 nm (d) and wavelength 1550 nm (e) as a function of incidence angle. Simulation results of the field distributions across the unit cell at 1550 nm (c) and 1250 nm wavelength (f) incidence. Dashed boxes represent the meta-atoms, and dash-dotted boxes represent the 1D photonic crystals.

1500 nm, and the thickness of the second layer of SU8 (l_3) is set to 500 nm. To introduce a bandgap edge in the near-infrared region, the thickness of Si in one basic unit of the 1D photonic crystal denoted as d_H is calculated as 70 nm, and the thickness of SiO_2 denoted as d_L is calculated as 170 nm according to the theory of photonic crystals [34]. The transmittance of 1D photonic crystals with a different layer number is simulated by commercial software (Lumerical FDTD Solutions). It can be found that four basic units stacked can make the bandgap edge sharp enough to realize the transmission–reflection modulation. Hence the total thickness of l_2 is 960 nm.

The 1D photonic crystal sandwiched between two layers of metasurfaces is the core of transmission and reflection control. In Fig. 3(a), we plot $\omega_n(k)$ $(n = 1,2)$ for the 1D photonic crystal mentioned above. A gap occurs between bands $n = 1$ and $n = 2$, at the Brillouin zone's edge. There is no allowed mode in the crystal that has a frequency within photonic bandgap, over the entire range of the Brillouin zone (we use ka/2π to label the horizontal axis shown in Fig. 3(a), where k is the wave vector). Thus, the transmittance of the frequency within the bandgap is close to zero. Figure 3(b) shows the transmittance and reflectance of the 1D photonic crystal in the near-infrared region, represented by the blue and red lines, respectively. Accordingly, the operating wavelength of transmission mode λ_1 is set to 1550 nm, which is outside the photonic bandgap, and the corresponding transmittance is 98.28%. The operating wavelength of reflection mode λ_2 is set to 1250 nm, which is inside the photonic bandgap, and the corresponding reflectance is 98.57%. The green-dotted box in Fig. 3(a) highlights the frequency range corresponding to the abscissa value shown in Fig. 3(b), thereby enhancing the clarity of their relationship. Figures 3(d) and 3(e) demonstrate the transmittance and reflectance as a function of the angle of incident light for the transmission and reflection operating wavelengths, respectively. For $\lambda_2 = 1250$ nm, a high reflectance of 84% can still be obtained when the incidence angle reaches

45°. A relatively high transmittance (greater than 71%) can be obtained, at wavelength $\lambda_1 = 1550$ nm, when the incidence angle is less than 25°. To visualize the mechanism of the full-space modulation of our design scheme, Figs. 3(c) and 3(f) show the simulated electric field distribution across the unit cell at 1550 nm and 1250 nm wavelength incidence, respectively.

Based on Eq. (1), the design method of a device with independent modulation of transmission and reflection EM space in the near-infrared region can be constructed by the following steps. The first is to select the meta-atoms in the bottom layer satisfying $\varphi_{bottom}(r, \lambda_2) = \varphi_R(r,\lambda_2)/2$ at wavelength λ_2 from the meta-unit library. Secondly, one should obtain the electromagnetic corresponding at wavelength λ_1 of the just selected meta-atoms $\varphi_{bottom}(r, \lambda_1)$. Thirdly, we can select the meta-atoms in the top layer metasurface, whose phase profile satisfies $\varphi_{top}(r, \lambda_1) = \varphi_T(r, \lambda_1) - \varphi_{bottom}(r, \lambda_1)$, and then the top layer and the bottom layer of the metasurface jointly satisfy the phase profile $\varphi_T(r, \lambda_1)$ at wavelength λ_1.

As a proof of concept, we start by designing a full-space device with a diameter of 40 μm, which can focus the transmitted light and reflected to a vortex beam with numerical apertures (NA) of 0.6 and 0.3 at λ_1 and λ_2, respectively. To achieve this, the phase profiles of transmission mode and reflection mode should be

$$\begin{cases} \varphi_T(r,\lambda_1) = -n_T \dfrac{2\pi}{\lambda_1}\left(\sqrt{r^2 + {f_T}^2} - f_T\right) \\ \varphi_R(r,\lambda_2) = -n_R \dfrac{2\pi}{\lambda_2}\left(\sqrt{r^2 + {f_R}^2} - f_R\right) + l\theta \end{cases}, \tag{2}$$

where n_T and n_R are the refractive indices of the transmission and reflection spaces, respectively, r is the radial axis, θ is the azimuthal angle, l is the topological charge (set as –1), and f_T and f_R are the focal lengths of the transmission and reflection modes (set as 34 μm and 67 μm, respectively).

According to the design steps mentioned above, the meta-atoms in top and bottom layers of the metasurface are carefully selected such that both the phase distributions can satisfy Eq. (1). To characterize this full-space light propagation, we simulated the intensity distributions of the optical field in x–z plane in transmission and reflection modes, which are normalized against the maximum value in the pattern. Figures 4(a) and 4(b) show the intensity distribution in reflection and transmission spaces,

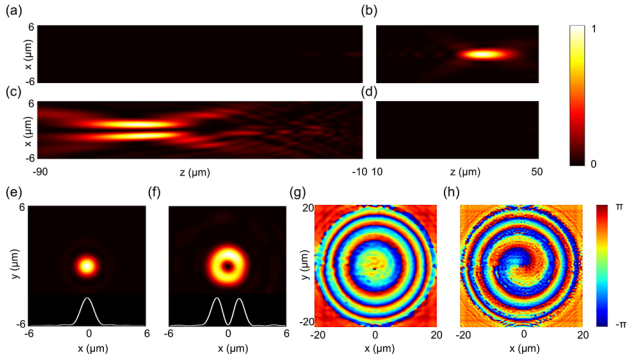

Fig. 4. Normalized intensity distribution in x–z plane of reflection space (a) and transmission space (b) in the transmission mode at wavelength λ_1. Normalized intensity distribution in x–z plane of reflection space (c) and transmission space (d) in the reflection space at wavelength λ_2. Normalized intensity distribution in the focal plane of the transmission mode (e) and the reflection mode (f). Near-field phase profile of transmitted wave (g) and reflected wave (h).

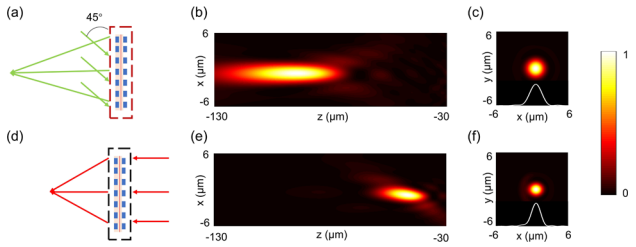

Fig. 5. Schematic of focusing the reflected wave with an incidence angle of 45° (a) and transmitted light with normal incidence (d). The black-dashed box represents the TRIM. Normalized intensity distribution in x–z plane in the reflection mode (b) and the transmission mode (e). Normalized intensity distribution in the focal plane of the reflection mode (c) and the transmission mode (f).

respectively, in the transmission mode at wavelength λ_1. We find that the transmitted waves are indeed well converged with a focal length of 36 μm, identified as the maximum field point in the $|E|^2 \sim z$ curve along the central z axis. The focal length identified agrees reasonably with the designed value of 34 μm. The intensity profiles of the focal plane and that along the x direction are depicted in Fig. 4(e). The full width at half maximum (FWHM) of the focal spot is 1.6 μm, in coincident with a diffraction limit focusing. The diffraction efficiency is 72.27%, which is calculated from the power in the focal spot (3 × FWHM) over that of the focal plane in the same area of metalens. Figure 4(g) shows the near-field phase profile of the device in the transmission mode. And the whole efficiency is 57.04%.

The characterization procedure in reflection mode is the same as that for the transmission mode. Figures 4(c) and 4(d) show the intensity distribution of reflection space and transmission space, respectively, in the reflection mode at wavelength λ_2. The focal length is identified as –65 μm, quite close to the designed value –67 μm. The intensity profiles of the focal plane and that along the x direction are also depicted in Fig. 4(f). The simulated phase profiles of the reflected wave are shown in Fig. 4(h). It can be observed that the spiral phase of the reflected wave is counterclockwise as designed.

As shown in Figs. 4(c), 4(f), and 4(h), the amplitude null at the center area and the spiral phase show the characteristic of the vortex beam with the OAM mode $l = -1$. Therefore, the proposed full-space metalens can, respectively, realize focusing and vortex beams in transmission and reflection modes at two wavelengths independently.

As has been mentioned, the 1D photonic crystal has a high reflectance of 84% at large angle (45°) incidence, which shows potential applications in technologies with oblique incidences, e.g., AR. In this regard, the reflected light with oblique 45° incidence and the transmitted light with normal incidence can be modulated simultaneously. To demonstrate the potential extended application, a TRIM with a diameter of 40 μm, which can independently modulate the wave with 45° oblique incidence in reflection mode (Fig. 5(a)) and waves with normal incidence in transmission mode (Fig. 5(d)), was designed and characterized. The phase profile of the transmission mode and reflection mode can be expressed as

$$\begin{cases} \varphi_T(r,\lambda_1) = -n_T \dfrac{2\pi}{\lambda_1}\left(\sqrt{r^2 + {f_T}^2} - f_T\right) \\ \varphi_R(r,\lambda_2) = -n_R \dfrac{2\pi}{\lambda_2}\left(\sqrt{r^2 + {f_R}^2} - f_R\right) - \dfrac{\sqrt{2}}{2} n_R x \end{cases}, \tag{3}$$

where f_T and f_R are set to –50 μm and –100 μm, respectively.

The normalized intensity distribution in x–z plane in the reflection mode and the transmission mode are shown in Figs. 5(b) and 5(e), respectively. The focal length is identified as –94.6 μm and –50.2 μm, quite close to the designed value –100 μm and –50 μm. Figures 5(c) and 5(f) show the intensity distribution in the corresponding focal plane of reflection and transmission modes, respectively. The above results prove the feasibility of this scheme in technologies with incident angle requirements.

In this Letter, we successfully designed the polarization-insensitive TRIM in the optical region with two channels at different wavelengths. It should be mentioned that four independent channels, specifically for transmission, reflection, and two orthogonal polarizations, can be achieved if the four-fold symmetric meta-atoms are replaced by anisotropic or chiral ones, which can further improve the multifunctional multiplexing capability of the device. Apart from acting as a dichroic filter, we could also design the 1D photonic crystal for other functions, such as introducing a defect layer in the middle to realize a bandpass filter [e.g., Ref. 6] and so on. The TRIM we have designed can be fabricated through e-beam lithography (EBL) and plasma-enhanced chemical vapor deposition (PECVD). The combination of the bilayer metasurface and the photonic crystal provides more degrees of freedom and flexibility for the design of full-space multifunctional multiplexing devices.

In summary, we have proposed a complete design for devices that can achieve full-space wavefront control in the optical region with the bilayer metasurface sandwiched by the 1D photonic crystal. To validate our method, two proof-of-concept designs were proposed and simulated, demonstrating the powerful capability of full-space modulation and the potential application of our design method. This design provides a promising way to realize the full-space control of electromagnetic waves and further facilitates the integration of optical devices and systems.

Funding. National Key Research and Development Program of China (2022YFA1404301); National Natural Science Foundation of China (62288101, 62305149, 62325504, 92250304).

Acknowledgments. Tao Li thanks the support from Dengfeng Project B of Nanjing University.

Disclosures. The authors declare no conflicts of interest.

Data availability. Data underlying the results presented in this paper are not publicly available at this time but may be obtained from the authors upon reasonable request.

REFERENCES

1. N. Yu, P. Genevet, M. A. Kats, F. Aieta, J.-P. Tetienne, F. Capasso, and Z. Gaburro, Science **334**, 333 (2011).
2. H.-H. Hsiao, C. H. Chu, and D. P. Tsai, Small Methods **1**, 1600064 (2017).
3. M. Khorasaninejad, W. T. Chen, R. C. Devlin, J. Oh, A. Y. Zhu, and F. Capasso, Science **352**, 1190 (2016).
4. T. Li, C. Chen, X. J. Xiao, J. Chen, S. S. Hu, and S. Ning Zhu, Photonics Insights **2**, R01 (2023).
5. Y. H. Chu, X. J. Xiao, X. Ye, C. Chen, S. N. Zhu, and T. Li, Opt. Express **31**, 21399 (2023).
6. H. Li, X. Xiao, B. Fang, S. Gao, Z. Wang, C. Chen, Y. Zhao, S. Zhu, and T. Li, Photonics Res. **9**, 1384 (2021).
7. S. Wang, P. C. Wu, V.-C. Su, Y.-C. Lai, M.-K. Chen, H. Y. Kuo, B. H. Chen, Y. H. Chen, T.-T. Huang, J.-H. Wang, R.-M. Lin, C.-H. Kuan, T. Li, Z. Wang, S. Zhu, and D. P. Tsai, Nat. Nanotechnol. **13**, 227 (2018).
8. G. Qu, W. Yang, Q. Song, Y. Liu, C.-W. Qiu, J. Han, D.-P. Tsai, and S. Xiao, Nat. Commun. **11**, 5484 (2020).
9. Y. W. Huang, W. T. Chen, W. Y. Tsai, P. C. Wu, C. M. Wang, G. Sun, and D. P. Tsai, Nano Lett. **15**, 3122 (2015).
10. X. Ye, X. Qian, Y. Chen, R. Yuan, X. Xiao, C. Chen, W. Hu, C. Huang, S. Zhu, and T. Li, Adv. Photonics **4**, 046006 (2022).
11. C. Chen, X. Ye, J. Sun, Y. Chen, C. Huang, X. Xiao, W. Song, S. Zhu, and T. Li, Optica **9**, 12 (2022).
12. X. Luo, Sci. China Phys. Mech. Astron. **58**, 594201 (2015).
13. M. Pu, X. Li, X. Ma, Y. Wang, Z. Zhao, C. Wang, C. Hu, P. Gao, C. Huang, and H. Ren, Sci. Adv. **1**, e1500396 (2015).
14. C. Zeng, H. Lu, D. Mao, Y. Q. Du, H. Hua, W. Zhao, and J. L. Zhao, Opto-Electron. Adv. **5**, 200098 (2022).
15. J. Chen, X. Ye, S. Gao, Y. Chen, Y. Zhao, C. Huang, K. Qiu, S. Zhu, and T. Li, Optica **9**, 431 (2022).
16. B. Xu, H. Li, S. Gao, X. Hua, C. Yang, C. Chen, F. Yan, S. Zhu, and T. Li, Adv. Photonics **2**, 066004 (2020).
17. P. Lin, W. T. Chen, K. M. A. Yousef, J. Marchioni, A. Zhu, F. Capasso, and J. X. Cheng, APL Photonics **6**, 096107 (2021).
18. W. Luo, S. Xiao, Q. He, S. Sun, and L. Zhou, Adv. Opt. Mater. **3**, 1102 (2015).
19. I. Yulevich, E. Maguid, N. Shitrit, D. Veksler, V. Kleiner, and E. Hasman, Phys. Rev. Lett. **115**, 205501 (2015).
20. W. Zhu, Q. Song, L. Yan, W. Zhang, P.-C. Wu, L. K. Chin, H. Cai, D. P. Tsai, Z. X. Shen, T. W. Deng, S. K. Ting, Y. Gu, G. Q. Lo, D. L. Kwong, Z. C. Yang, R. Huang, A. Q. Liu, and N. Zheludev, Adv. Mater. **27**, 4739 (2015).
21. N. K. Grady, J. E. Heyes, D. R. Chowdhury, Y. Zeng, M. T. Reiten, A. K. Azad, A. J. Taylor, D. A. R. Dalvit, and H. T. Chen, Science **340**, 1304 (2013).
22. T. Cai, G. Wang, S. Tang, H. Xu, J. Duan, H. Guo, F. Guan, S. Sun, Q. He, and L. Zhou, Phys. Rev. Appl. **8**, 034033 (2017).
23. L. Bao, Q. Ma, R. Y. Wu, X. Fu, J. Wu, and T. J. Cui, Adv. Sci. **8**, 2100149 (2021).
24. Y. Zhuang, G. Wang, T. Cai, and Q. Zhang, Opt. Express **26**, 3594 (2018).
25. J. N. Yang, X. Y. Wu, J. K. Song, C. Huang, Y. J. Huang, and X. G. Luo, Opt. Express **27**, 9061 (2019).
26. H. C. Zhang, X. Zhang, X. L. Ma, M. Pu, C. Huang, Z. J. Zhang, Y. X. Wang, Y. H. Guo, J. Luo, and X. G. Luo, Opt. Express **30**, 36949 (2022).
27. J. Wang, Z. Zhang, C. Huang, M. Pu, X. Lu, X. Ma, Y. Guo, J. Luo, and X. Luo, Adv. Opt. Mater. **10**, 2102111 (2022).
28. P. Xu, H. X. Liu, R. J. Li, J. Q. Han, S. L. Chen, and L. Li, Adv. Opt. Mater. **1**, 2203117 (2023).
29. L. Zhang, R. Y. Wu, G. D. Bai, H. T. Wu, Q. Ma, X. Q. Chen, and T. J. Cui, Adv. Funct. Mater. **28**, 1802205 (2018).
30. C. Kim, S. Kim, and B. Lee, Opt. Express **28**, 18059 (2020).
31. Y. L. Wang, Q. B. Fan, and T. Xu, Opto-Electron. Adv. **4**, 200008 (2021).
32. W. B. Feng, J. C. Zhang, Q. F. Wu, A. Martins, Q. Sun, Z. H. Liu, Y. Long, E. R. Martins, J. T. Li, and H. W. Liang, Nano Lett. **22**, 3969 (2022).
33. Y. J. Bao, F. Nan, J. H. Yan, X. G. Yang, C. W. Qiu, and B. J. Li, Nat. Commun. **13**, 7550 (2022).
34. D. J. John, G. J. Steven, and D. M. Robert, *Photonic Crystals Molding the Flow of Light*, 2nd Ed. (Princeton University Press, 2008).